

Deep-learning jet flavor tagging for precision hadronic Higgs measurements at future e^+e^- Higgs factories

Xinzhu Wang,^{a,c,†} Yifan Zhu,^{b,c,†} Chunxiang Zhu,^{a,c} Jianfeng Jiang,^{d,e} Manqi Ruan,^{d,e} Kun Wang,^{f,*} Haijun Yang,^{a,b,c,*} Yongfeng Zhu^{d,e}

^a*Institute of Nuclear and Particle Physics, School of Physics and Astronomy, Shanghai Jiao Tong University, Shanghai 200240, China*

^b*Tsung-Dao Lee Institute, Shanghai Jiao Tong University, Shanghai 200240, China*

^c*National Key Laboratory of Dark Matter Physics, Shanghai Key Laboratory for Particle Physics and Cosmology, Key Laboratory for Particle Astrophysics and Cosmology (MoE), Shanghai 200240, China*

^d*Institute of High Energy Physics, Chinese Academy of Sciences, Beijing 100049, China*

^e*University of Chinese Academy of Sciences, 19A Yuquan Road, Beijing 100049, China*

^f*College of Science, University of Shanghai for Science and Technology, Shanghai 200093, China*

E-mail: kwang@usst.edu.cn, haijun.yang@sjtu.edu.cn

ABSTRACT: Precise measurements of Higgs decays into quarks and gluons are essential for probing the Yukawa couplings of the Higgs boson and testing the flavor structure of the Standard Model. We investigate the process $e^+e^- \rightarrow ZH$ at $\sqrt{s} = 240$ GeV at a future e^+e^- Higgs factory, taking the CEPC design as a benchmark. The analysis focuses on events with $Z \rightarrow \nu\bar{\nu}$ and hadronic Higgs decays $H \rightarrow b\bar{b}, c\bar{c}, s\bar{s}$ and gg . Jet flavor is identified using state-of-the-art particle-level deep neural network taggers (ParticleNet, Particle Transformer and More-Interaction Particle Transformer), whose per-jet outputs are combined with global event observables in a two-stage analysis employing XGBoost classifiers to separate the four Higgs decay modes from the dominant two- and four-fermion Standard Model backgrounds. Assuming an integrated luminosity of 20 ab^{-1} , we obtain projected relative precision on $\sigma(ZH) \times \text{Br}(H \rightarrow X)$ of 0.18% for $X = b\bar{b}$, 1.07% for $c\bar{c}$, 0.52% for gg and 78% for $s\bar{s}$. Compared with the CEPC published results, the precisions for $H \rightarrow c\bar{c}$ and $H \rightarrow gg$ are improved by about 42% and 26%, respectively. For $H \rightarrow s\bar{s}$ we present a quantitative sensitivity estimation corresponding to a statistical significance of about 1.3σ . These results highlight the potential of deep-learning-based jet flavor tagging for precision studies of Higgs decays at future e^+e^- Higgs factories.

[†]These authors contributed equally to the work.

*Corresponding author.

Contents

1	Introduction	1
2	Simulation and analysis strategy	3
2.1	Simulation setup and event samples	3
2.2	Two-stage jet and event-level analysis	5
3	Results and discussions	8
3.1	Jet-level performance	8
3.2	Event-level classification performance	10
3.3	Physics interpretation of the event-level classifier	11
3.4	Expected sensitivities and discussion	12
4	Conclusions	15
A	Preselection kinematics	17
B	Event-level classifier details	19
B.1	XGBoost setup and training strategy	19
B.2	Physics interpretation	19
C	Comparison with holistic event-level classification	24

1 Introduction

The discovery of the Higgs boson at the Large Hadron Collider (LHC) by the ATLAS and CMS Collaborations [1, 2] completed the particle content predicted by the Standard Model (SM) and confirmed the mechanism of electroweak symmetry breaking [3–7]. Over the past decade, a broad program of precision measurements has examined the Higgs couplings to weak gauge bosons and third-generation fermions through various decay channels, including $H \rightarrow WW/ZZ$ [2, 8, 9], $H \rightarrow \gamma\gamma$ [8, 10], $H \rightarrow b\bar{b}$ [11, 12], and $H \rightarrow \tau^+\tau^-$ [13, 14]. These results are in excellent agreement with SM predictions within the current experimental uncertainties. However, some crucial aspects of the Higgs sector remain unexplored, particularly its interactions with second-generation fermions such as $H \rightarrow s\bar{s}$.

In the SM, the Yukawa couplings of the Higgs to second-generation fermions are suppressed relative to the third generation, leading to rare decay modes such as $H \rightarrow c\bar{c}$, $H \rightarrow s\bar{s}$, and $H \rightarrow \mu^+\mu^-$. While emerging evidence for $H \rightarrow c\bar{c}$ [15] and $H \rightarrow \mu^+\mu^-$ [16, 17] has been reported at the LHC, direct measurements of the light quark channels remain challenging. This is primarily due to the overwhelming quantum chromodynamics (QCD) background in hadronic environments [18], where jets originating from c and s quarks must

be distinguished from a large number of jets initiated by u/d quarks and gluons, which exhibit similar substructure. Nevertheless, precision measurements of these rare decays are essential not only to examine the Higgs mechanism but also to test the SM to its limits and probe possible extensions, such as models featuring modified Yukawa hierarchies or flavor-violating Higgs interactions [19–22].

Future electron-positron (e^+e^-) colliders, such as the Circular Electron-Positron Collider (CEPC) [23–26], the Future Circular Collider-ee (FCC-ee) [27] and the International Linear Collider (ILC) [28], are designed to operate as high-luminosity ‘Higgs factories’. These colliders offer a clean experimental environment with precise initial-state control, low pileup and minimal QCD backgrounds, making them ideal for precision Higgs measurements that are extremely difficult at hadron colliders. Specifically, the $e^+e^- \rightarrow ZH$ process with Z decaying into $\nu\bar{\nu}$ provides a clean final-state topology, where the Higgs boson recoils against the missing momentum, allowing easier isolation of hadronic Higgs decays with minimal background contamination. While this work uses the CEPC detector and luminosity assumptions as a benchmark, the developed analysis methodology is broadly applicable to other future e^+e^- Higgs factories.

A key challenge in studying hadronic Higgs decays is jet flavor tagging. In the ZH events considered in this paper, Higgs decaying into quarks or gluons appear as two collimated jets. The flavors, or the origins of these jets are essential to distinguishing between different Higgs decay modes, such as $H \rightarrow b\bar{b}$, $c\bar{c}$, $s\bar{s}$ and gg , and to separating them from background processes. At the LHC, modern machine learning algorithms like GN2 [29] and DeepJet [30] have achieved excellent performance in identifying b - and c -jets, but they struggle to separate light-flavor jets (s -, u -, d -jets and gluon jets), which typically lack distinctive displaced vertices. This limitation presents a significant obstacle to accurately measuring $H \rightarrow s\bar{s}$ and to improving the precision for $H \rightarrow c\bar{c}$ and $H \rightarrow gg$.

To address these challenges, current state-of-the-art deep learning models, such as ParticleNet (PN) [31], Particle Transformer (ParT) [32], and More-Interaction Particle Transformer (MIParT) [33], operate directly on the particle-level information of each jet. By considering the relationships between particles within each jet, these newer models are able to capture more complex patterns of interaction, which is crucial for distinguishing jets originating from light-flavor quarks even in the presence of significant QCD backgrounds. To further improve signal-background separation, we combine the outputs of these three deep learning models with an event-level classifier, XGBoost [34–36]. This two-stage classification approach allows us to effectively separate Higgs decays from backgrounds by exploiting both jet-level information and global event kinematics.

In this work, we provide a systematic sensitivity estimate for $H \rightarrow s\bar{s}$ at a lepton collider, alongside updated precision projections for other hadronic Higgs decays. We show that, with the proposed tagging methods, the projected precision for $\sigma(ZH) \times \text{Br}(H \rightarrow c\bar{c})$ and $\sigma(ZH) \times \text{Br}(H \rightarrow gg)$ improves by about 42% and 26%, respectively, compared with the CEPC published results [37]. For $H \rightarrow s\bar{s}$, we provide a benchmark sensitivity of 1.3σ for single $ZH \rightarrow \nu\nu s\bar{s}$ channel, marking a significant step towards probing the strange Yukawa coupling.

This paper is organized as follows. In Sec. 2 we describe the collider and detector setup,

event generation, jet reconstruction and flavor tagging, as well as the event selection and multivariate analysis strategy. Section 3 presents the jet- and event-level performance and the projected sensitivities to $\sigma(ZH) \times \text{Br}(H \rightarrow b\bar{b}, c\bar{c}, gg, s\bar{s})$, including a comparison with the CEPC Higgs benchmark [37] and FCC-ee projections [38]. We conclude and discuss future prospects in Sec. 4.

2 Simulation and analysis strategy

In this section, we describe the collider and detector assumptions, the Monte Carlo (MC) simulation, jet reconstruction and flavor tagging, and the event-level classification strategy used to obtain the projections presented in the following. We take the CEPC as a concrete benchmark of a high-luminosity Higgs factory, but the analysis chain is otherwise generic and can be straightforwardly reinterpreted for other future e^+e^- colliders.

2.1 Simulation setup and event samples

The CEPC is designed to operate at $\sqrt{s} = 240$ GeV and to collect an integrated luminosity of 20 ab^{-1} in Higgs factory mode, corresponding to four million Higgs bosons produced in association with a Z boson [26, 39, 40]. The reference detector features a low-mass silicon vertex detector and tracker [41], surrounded by highly granular electromagnetic and hadronic calorimeters optimized for particle-flow reconstruction [42]. This configuration provides excellent impact-parameter resolution, jet-energy and angular resolution, and particle identification capabilities, which are all critical for heavy- and light-flavor jet tagging.

Hard-scattering events are generated with WHIZARD 1.95 [43], including initial-state radiation, and interfaced with PYTHIA 6.4 [44] for parton showering and hadronization. Detector effects are simulated with DELPHES3 [45] using the official CEPC detector card, which parametrizes the tracking efficiency, momentum and impact-parameter resolutions, calorimeter responses and the performance of particle-flow reconstruction. Unless stated otherwise, all projections are normalized to an integrated luminosity of 20 ab^{-1} at $\sqrt{s} = 240$ GeV.

The signal process considered in this work is the associated Higgs production

$$e^+e^- \rightarrow ZH, \quad Z \rightarrow \nu\bar{\nu}, \quad H \rightarrow q\bar{q} \text{ or } H \rightarrow gg, \quad (2.1)$$

where the Higgs boson decays hadronically and the Z boson decays invisibly. We explicitly simulate the Higgs decay modes $H \rightarrow b\bar{b}, c\bar{c}, s\bar{s}, gg, u\bar{u}$, and $d\bar{d}$, with the production cross sections and decay branching ratios taken from Refs. [46, 47]. The dominant non-Higgs backgrounds are two-fermion ($2f$) and four-fermion ($4f$) processes, in particular $e^+e^- \rightarrow q\bar{q}$ and $e^+e^- \rightarrow \nu\bar{\nu}q\bar{q}$. We also include the Higgs-associated background where the pair of Z bosons originating from the Higgs boson decay invisibly and hadronically respectively. Representative Feynman diagrams for the signal and the main background topologies are shown in Fig. 1.

The MC samples used in this analysis are summarized in Table 1. For each Higgs decay mode we generate 10^7 events, corresponding to negligible MC statistical uncertainty

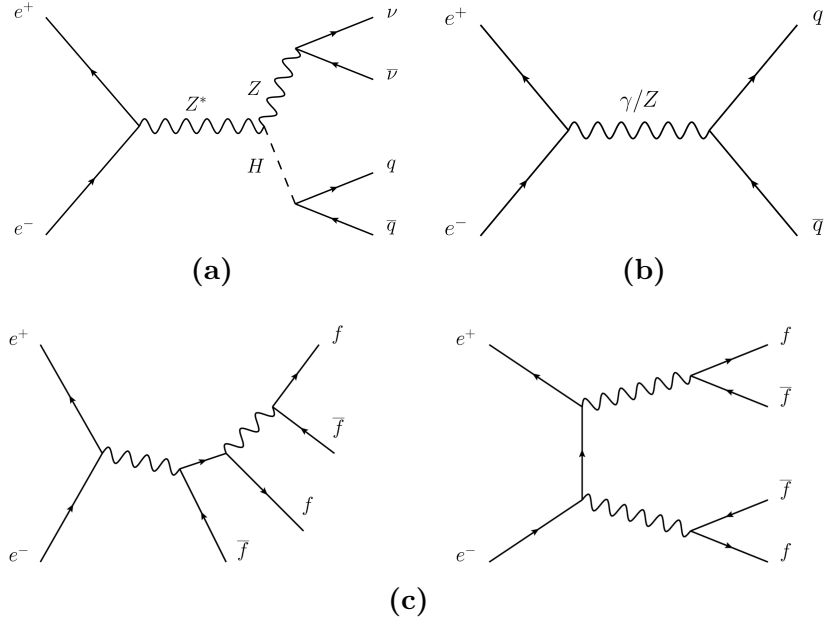


Figure 1. Representative Feynman diagrams for the signal and background processes: (a) $e^+e^- \rightarrow ZH$ with $Z \rightarrow \nu\bar{\nu}$ and $H \rightarrow q\bar{q}$; (b) the two-fermion background $e^+e^- \rightarrow q\bar{q}$; (c) the representative four-fermion background $e^+e^- \rightarrow \nu\bar{\nu}q\bar{q}$.

Table 1. Cross sections and simulated events for signal and background processes. For all signal samples the production mode is $e^+e^- \rightarrow ZH$ with $Z \rightarrow \nu\bar{\nu}$; major backgrounds include four-fermion and two-fermion processes. For the two-fermion samples, the quoted cross sections are evaluated after the generator-level event filter with an efficiency of about 2%.

Category	Channel	σ [fb]	N_{exp} [k]	N_{MC} [k]
Signal	$e^+e^- \rightarrow ZH, Z \rightarrow \nu\bar{\nu}, H \rightarrow b\bar{b}$	26.71	534.2	10000
	$e^+e^- \rightarrow ZH, Z \rightarrow \nu\bar{\nu}, H \rightarrow c\bar{c}$	1.35	27.0	10000
	$e^+e^- \rightarrow ZH, Z \rightarrow \nu\bar{\nu}, H \rightarrow s\bar{s}$	0.01	0.2	10000
	$e^+e^- \rightarrow ZH, Z \rightarrow \nu\bar{\nu}, H \rightarrow gg$	3.97	79.4	10000
	$e^+e^- \rightarrow ZH, Z \rightarrow \nu\bar{\nu}, H \rightarrow u\bar{u}$	2.77×10^{-5}	0.00056	10000
	$e^+e^- \rightarrow ZH, Z \rightarrow \nu\bar{\nu}, H \rightarrow d\bar{d}$	8.00×10^{-3}	0.16	10000
Background	$e^+e^- \rightarrow \nu\bar{\nu}H, H \rightarrow ZZ^* \rightarrow \nu\bar{\nu}q\bar{q}$	0.34	6.8	10000
	$e^+e^- \rightarrow 4f$	369.71	7394.2	44000
	$e^+e^- \rightarrow 2f$	1213.25	24265.0	6000

in the subsequent training of the jet taggers. For the $2f$ processes, generator-level phase-space cuts ($110 < m_{q\bar{q}} < 140$ GeV and $15 < p_{\text{T}}(q) < 100$ GeV) are applied to enhance the acceptance in the kinematic region relevant for the $ZH(\nu\bar{\nu})$ topology, resulting in a selection efficiency of about 2% applied to the cross section quoted in the Table 1. The channels $H \rightarrow u\bar{u}$ and $H \rightarrow d\bar{d}$ have cross sections several orders of magnitude smaller than $H \rightarrow s\bar{s}$ and are therefore not included in the event-level signal extraction; however, they are kept in the jet-tagging training in order to stabilize the light-flavor classification. Contributions from $H \rightarrow WW^*$ are effectively suppressed by the lepton veto used in the event selection and are neglected in this analysis, consistent with Ref. [48].

2.2 Two-stage jet and event-level analysis

Jets are reconstructed from all stable visible particles (excluding neutrinos) using the ee - k_t algorithm [49], following the CEPC baseline strategy. Each event contains exactly two reconstructed jets, which are taken as Higgs decay products and are used as inputs to the jet flavor taggers.

A central ingredient of the analysis is the identification of the jet flavor originating from the Higgs decay. Instead of relying on hand-crafted high-level observables, we employ three state-of-the-art particle-level deep neural networks: PN, ParT and MIParT. Each jet is represented as an unordered set of reconstructed particles, characterized by per-particle kinematics, particle-identification (PID) flags and track-trajectory information as listed in Table 2. PN is based on dynamic graph convolutions and is particularly effective at learning local substructure features; ParT employs transformer-style attention to capture long-range correlations between particles within jets; MIParT simplifies the attention mechanism to increase efficiency while retaining strong representational power for particle interactions. Each jet is assigned one of 11 labels by these networks: b , \bar{b} , c , \bar{c} , s , \bar{s} , u , \bar{u} , d , \bar{d} , or g , and the performance of the taggers is quantified using multi-class confusion matrices, which will be discussed in Sec. 3.

The input features used for jet tagging are summarized in Table 2. They consist of: (i) particle-level kinematic quantities, defined relative to the jet axis and normalized by the jet transverse momentum or energy; (ii) binary PID indicators provided by Delphes3; and (iii) impact-parameter related observables for charged tracks, which encode information on

Table 2. Input feature categories used for training the jet-tagging networks.

Kinematics	Particle identification	Trajectory
$\Delta\eta$	charged kaon	$\tanh d_0$
$\Delta\phi$	pion	$\tanh d_z$
$\log p_{\text{T}}$	charged hadron	$\tanh \sigma_{d_0}$
$\log E$	neutral hadron	$\tanh \sigma_{d_z}$
$\log(p_{\text{T}}/p_{\text{T}}^{(\text{jet})})$	electron	
$\log(E/E^{(\text{jet})})$	muon	
ΔR	photon	

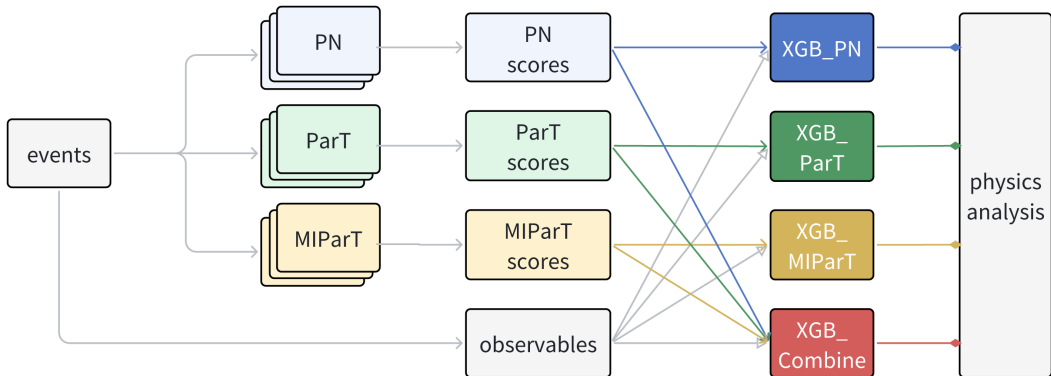


Figure 2. Schematic overview of the analysis strategy. Events are first processed by the three jet-level taggers (PN, ParT, MIParT). Their per-jet flavor scores, together with global event observables, are then used as inputs to a set of XGBoost classifiers: three using a single tagger each (XGB_PN, XGB_ParT, XGB_MIParT) and one combined classifier (XGB_Combine) that combines all three taggers simultaneously.

displaced vertices. Before being fed into the networks, all features are standardized using the mean and standard deviation computed from the training sample. For each jet tagger, we train three independent models with different random initializations, in order to assess the stability of the results. Approximately 25% of the signal events are reserved for the development and evaluation of the jet tagging networks, while the remaining 75% are kept for the event-level analysis described below. Background samples are excluded from the jet tagging procedure.

The overall analysis follows a hierarchical two-stage design, illustrated schematically in Fig. 2. At the jet level, three deep-learning jet taggers, PN, ParT and MIParT, are trained to predict per-jet flavor labels, each repeated three times using different training initializations to ensure statistical robustness. These jet-level outputs, together with global event observables, serve as inputs to subsequent event-level classifiers. This modular structure decouples microscopic jet-substructure learning from event-level correlations, enhancing both sensitivity and interpretability.

On top of the jet-level flavor information, we exploit global event kinematics to enhance the separation between different Higgs decay modes and backgrounds. After reconstructing the jets and evaluating the PN, ParT and MIParT outputs for the two Higgs-candidate jets, we build a set of event-level observables including:

- Single-jet variables: Transverse and longitudinal momenta, pseudorapidity and polar angle of the leading and subleading jets.
- Dijet system variables: Invariant mass and angular separations ($\Delta\eta_{jj}$, $\Delta\phi_{jj}$, $\Delta\theta_{jj}$) of the jet pair;
- Missing energy (ME) related variables: The transverse and longitudinal components of the missing energy (MET and MEZ) and its polar and azimuthal angles (η_{ME} ,

Table 3. Inputs for XGBoost classification.

Category	Features
Single-jet kinematics	$p_T, p_z, \eta, \theta, \phi, \text{energy}$
Jet shape and composition	$n_{\text{particles}}, \Delta R, \Delta p_T$
Dijet kinematics	$m_{jj}, \Delta\eta_{jj}, \Delta\theta_{jj}, \Delta\phi_{jj}$
Missing energy	$\text{MET}, \text{MEZ}, \eta_{\text{ME}}, \theta_{\text{ME}}, \phi_{\text{ME}}, \text{MET}/H_T$
Jet–MET correlations	$\Delta\eta, \Delta\phi, \Delta\theta$ between each jet and MET
Jet flavor tagging scores	outputs from ParticleNet, ParT, and MIParT

θ_{ME} and ϕ_{ME}) and the ratio between MET and the scalar sum of p_T of the jets (MET/H_T).

- Correlations between each jet and MET, including $\Delta\eta(j, \text{MET}), \Delta\phi(j, \text{MET})$ and $\Delta\theta(j, \text{MET})$;
- The jet flavor tagging outputs of PN, ParT and MIParT for each of the jets, which summarize the microscopic substructure information learned at the jet level.

A representative list of these observables is given in Table 3. A quantitative study of the relative importance of these input variables in this analysis, based on feature importance and SHAP[50] values, is presented in Appendix B.2. Before multivariate training, a loose preselection is applied to enhance the $ZH(\nu\bar{\nu})$ topology while keeping high signal efficiency. In particular, we require the leading jet to satisfy $p_T \in (15, 100)$ GeV and $p_z \in (-95, 95)$ GeV, the missing longitudinal energy to be within $E_{z,\text{miss}} \in (-55, 55)$ GeV, and the dijet invariant mass to lie in the window $m_{jj} \in (110, 140)$ GeV. These requirements retain about 80% of the Higgs signal while rejecting more than 97% of the inclusive $2f$ and $4f$ backgrounds. The corresponding kinematic distributions for signal and background processes, and their physical interpretation, are discussed in Appendix A.

Event-level classification is performed using the XGBoost algorithm [36], a gradient-boosted decision-tree method [34, 35] well suited for heterogeneous inputs and for combining deep-learning-based jet information with classical event-level kinematic observables. We train six-class classifiers to distinguish $H \rightarrow b\bar{b}, H \rightarrow c\bar{c}, H \rightarrow s\bar{s}, H \rightarrow gg$, and the $2f$ and $4f$ backgrounds. All classifiers make use of the same set of event-level kinematic observables. The three baseline models differ only in the source of jet-level information, each using the per-jet scores from a single tagger (XGB_PN, XGB_ParT, and XGB_MIParT). A fourth classifier, XGB_Combined, is trained using the full collection of jet scores from all three taggers together, in addition to the same kinematic observables, allowing XGBoost to exploit the complementary information among them. For each classifier, the event-level samples are randomly split into statistically independent training, validation and test sets in a 6:2:2 ratio. Hyperparameters such as the maximum tree depth, learning rate and number of boosting rounds are tuned on the validation sample to optimize the multi-class log-loss and to avoid overfitting. The resulting classifier outputs are used in Sec. 3 to

define signal-enriched regions for each Higgs decay channel and to extract the projected measurement precisions.

For the purpose of signal extraction, the output score of a given XGBoost classifier is treated as a one-dimensional discriminant for the corresponding Higgs decay hypothesis. For each channel, all other Higgs decays as well as the $2f$ and $4f$ processes are considered as background. After normalizing the samples to 20 ab^{-1} , we scan over possible thresholds on the classifier score and, for each threshold, compute the expected numbers of signal (S) and background (B) events. The statistical significance is evaluated using the profile-likelihood approximation

$$Z = \sqrt{2 \left[(S + B) \ln \left(1 + \frac{S}{B} \right) - S \right]}, \quad (2.2)$$

and the optimal working point is chosen as the threshold that maximizes Z . The corresponding efficiencies and event yields serve as the basis for the precision and sensitivity estimates presented in Sec. 3.

3 Results and discussions

In this section we present the performance of the jet-level flavor taggers and of the event-level classifiers, and derive the expected sensitivities to hadronic Higgs decays at CEPC Higgs factory. Unless stated otherwise, all results are normalized to an integrated luminosity of 20 ab^{-1} at $\sqrt{s} = 240 \text{ GeV}$.

3.1 Jet-level performance

The jet flavor taggers described in Sec. 2.2 are evaluated on an independent sample of $\nu\bar{\nu}H$ events, with $H \rightarrow q\bar{q}$ or $H \rightarrow gg$. Fig. 3 shows the resulting 11×11 confusion matrices for ParticleNet, ParT and MIParT, respectively. Each matrix element M_{ij} gives the fraction of jets with true flavor i that are assigned to flavor j by the classifier.

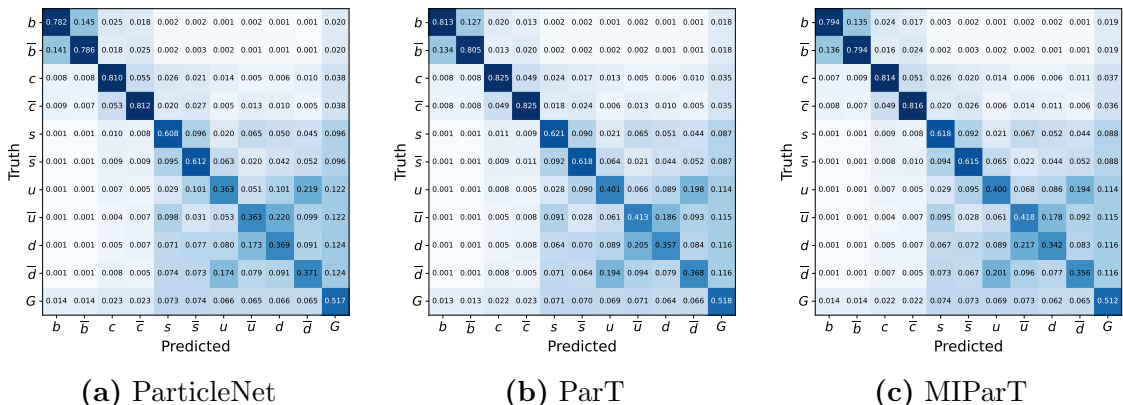


Figure 3. Jet identification confusion matrices for $\nu\bar{\nu}H$, $H \rightarrow q\bar{q}$ events from ParticleNet (a), ParT (b) and MIParT (c). Each entry gives the fraction of jets of true flavor i classified as flavor j .

All three taggers achieve a good separation between b - and c -jets and the other flavors. When particle and antiparticle jets are not distinguished, the effective b -tagging and c -tagging efficiencies exceed 90%, while misidentification of light-flavor jets as heavy flavors remains at the percent level. This confirms that the CEPC detector, together with the adopted vertexing and tracking performance, provides excellent heavy-flavor tagging capabilities.

For light-flavor jets, the task is intrinsically more challenging. When particle and antiparticle jets are not distinguished, the self-identification probability for strange jets is around 60–70%, and gluon jets are correctly classified in about half of the cases, with substantial migration among s , u/d and g categories. These patterns are expected, as strange and gluon jets share similar particle multiplicities and radial energy profiles, and differ only through relatively subtle fragmentation and PID information. The three taggers yield broadly comparable performance, with ParT and MIParT providing a modest improvement in heavy- and strange-flavor tagging efficiencies relative to ParticleNet, while ParticleNet achieves a similar performance on gluon jets. Overall, the differences are at the level of a few percentage points and will later be exploited through an ensemble combination at the event level.

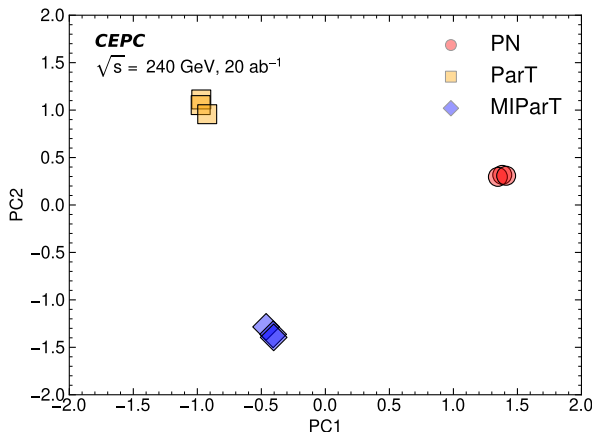


Figure 4. PCA projection of model-predicted s -jet probabilities for the $H \rightarrow s\bar{s}$ channel. Each point represents one independently trained model of ParticleNet (circles), ParT (squares) or MIParT (diamonds). Points of the same color correspond to the same model architecture, while the spread within a cluster reflects different training initializations. Models of the same architecture form compact clusters, indicating good training stability, while the separation between clusters reflects inter-architecture diversity that can be exploited in an ensemble.

To quantify the complementarity among the different taggers, we perform a principal-component analysis (PCA) [51] of their outputs to visualise the correlations between them. For each architecture, several independently trained models (with different random initializations) are used to predict the s -jet probability for jets in the $H \rightarrow s\bar{s}$ sample. The distributions of these probabilities are then projected onto the first two principal components. The result is shown in Fig. 4, where each point corresponds to one trained model.

Models of the same architecture cluster closely together in the PCA plane, demonstrating that the training procedure is stable and that statistical fluctuations from random initialization are small. By contrast, the clusters associated with PN, ParT and MIParT are clearly separated, indicating that the three taggers capture somewhat different aspects of the jet substructure. This inter-model diversity motivates the construction of the combined event-level classifier (`XGB_Combined`) that simultaneously uses the outputs of all three taggers, as discussed in the next subsection.

3.2 Event-level classification performance

The event-level XGBoost classifiers, introduced in Sec. 2.2, are trained to separate four Higgs decay modes ($H \rightarrow b\bar{b}$, $c\bar{c}$, $s\bar{s}$, gg) from the dominant $2f$ and $4f$ backgrounds. Fig. 5 summarizes the performance of the combined classifier, `XGB_Combined`, in the strange-enriched signal region.

The confusion matrix in the left panel shows that $H \rightarrow b\bar{b}$ and $H \rightarrow c\bar{c}$ are efficiently identified: the diagonal elements exceed 97% and 93% for $b\bar{b}$ and $c\bar{c}$ respectively, and the cross-contamination between these two modes is at the per-mille level. This reflects the strong discriminating power of the heavy-flavor taggers combined with kinematic differences among the channels.

The $H \rightarrow gg$ and $H \rightarrow s\bar{s}$ entries have diagonal elements of about 82% and 86%, respectively, with the largest off-diagonal migration occurring between these two channels. This less pronounced separation is driven by the similarity of the s - and g -jet topologies. The $2f$ and $4f$ backgrounds are efficiently controlled: the $2f$ class is identified with an

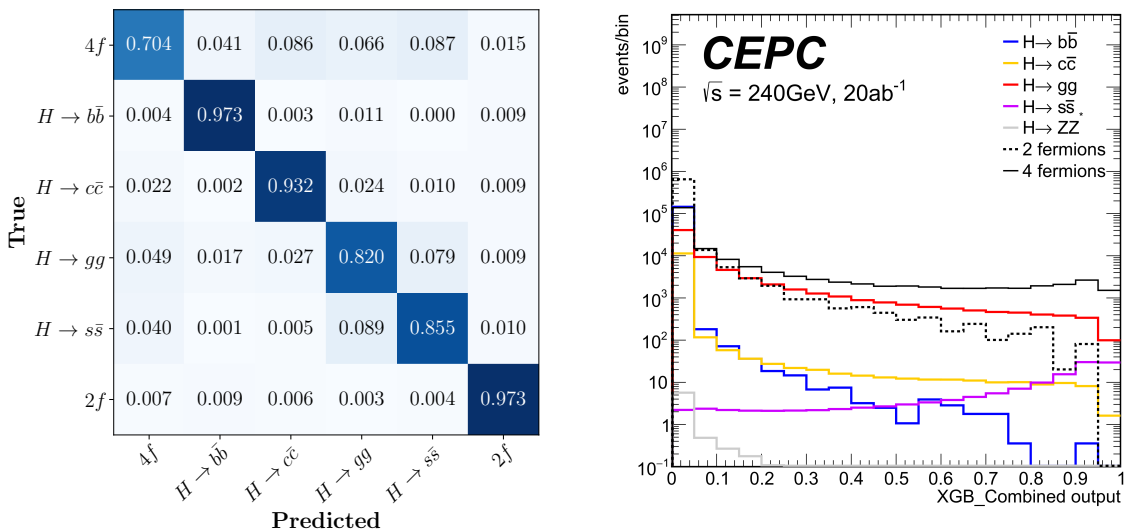


Figure 5. Performance of the XGBoost event classifier in the strange-enriched region. Left: confusion matrix for the `XGB_Combined` model, demonstrating clear separation for $H \rightarrow b\bar{b}$ and $H \rightarrow c\bar{c}$, while some confusion remains between $H \rightarrow s\bar{s}$ and $H \rightarrow gg$ due to similar jet substructure. Right: distribution of the `XGB_Combined` output score, taking $H \rightarrow s\bar{s}$ as signal, with all samples normalized to 20 ab^{-1} . Higher scores correspond to higher signal purity, and $4f$ processes constitute the dominant background.

accuracy of about 97%, and the $4f$ class with about 70%, the latter reflecting the broader kinematic variety of four-fermion final states.

The right panel of Fig. 5 displays the distribution of the `XGB_Combined` score when $H \rightarrow s\bar{s}$ is taken as the signal hypothesis. The signal events populate the high-score region, while the $4f$ background dominates at intermediate scores and the inclusive $2f$ background is largely confined to low scores. This behavior confirms that the classifier successfully leverages both jet-level flavor information and global event kinematics to construct a discriminant that is monotonic in signal purity.

3.3 Physics interpretation of the event-level classifier

For precision measurements, it is important to verify that the multivariate classifier exploits physically sensible information rather than behaving as an opaque black box. For the `XGB_Combined` model, we therefore inspect the relative importance of each input feature using the standard XGBoost gain metric, and we further check the behaviour with SHapley Additive exPlanations (SHAP) values [50]; a detailed discussion of the interpretation is given in Appendix B.2. Here we summarise the main points relevant for the physics interpretation.

Fig. 6 displays the twelve most important input variables for `XGB_Combined`, ranked by their total gain fraction. The two leading features are the ParT b - and c -jet scores of the leading jet, followed by the global observables MET/H_T and MET . The next group consists of the ParT gluon and strange scores and the PN b score for the subleading jet, together with additional ParT strange scores and the MIParT d score. This pattern confirms that heavy-flavor tagging provides the primary handle for isolating $H \rightarrow b\bar{b}$ and $H \rightarrow c\bar{c}$, while s - and g -jet information, especially for the subleading jet, is essential for separating $H \rightarrow s\bar{s}$

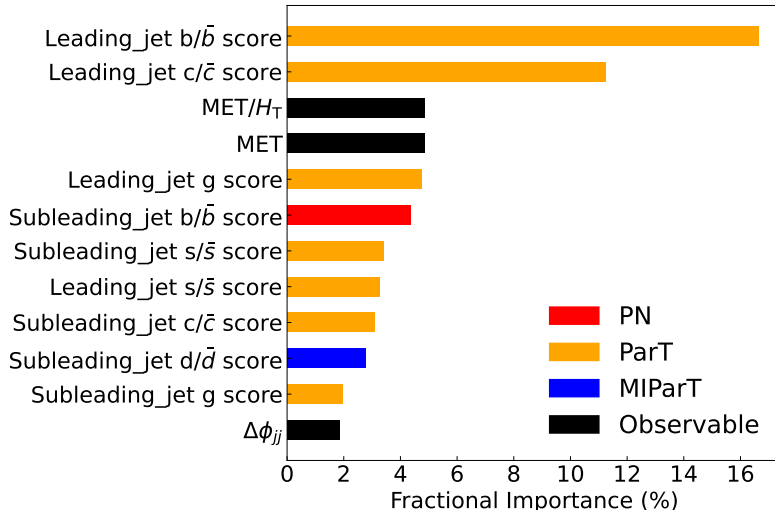


Figure 6. Top 12 most important input variables for the `XGB_Combined` classifier, ranked by their total gain fraction in the XGBoost ensemble. Entries are colour-coded according to their origin: PN, ParT, MIParT, or high-level kinematic observables. A more detailed ranking is given in Appendix B.2.

and $H \rightarrow gg$. The presence of PN and MIParT scores among the top features shows that the three jet taggers capture complementary aspects of the jet substructure, which the combined classifier can effectively exploit. Variables such as m_{jj} appear slightly below this leading set in the feature-importance ranking shown in Appendix B.2, but still provide useful additional discrimination.

The relative importance of the different taggers can be quantified by retraining the event-level classifier using only the ParT, MIParT or PN scores as jet inputs, while keeping the same set of kinematic observables. As summarised in Table 7 (Appendix B.2), using only the ParT scores already captures almost all of the tagging power. Including the PN and MIParT scores in the `XGB_Combined` setup leads to small but noticeable improvements, particularly for $H \rightarrow gg$ and $H \rightarrow s\bar{s}$, and reduces the spread among independent trainings (Fig. 7), indicating that the multi-architecture ensemble is most beneficial in the difficult, light-flavor channels.

A complementary, event-by-event view is provided by the per-class SHAP analysis in Appendix B.2. In brief, large b - or c -jet probabilities push events towards the $H \rightarrow b\bar{b}$ and $H \rightarrow c\bar{c}$ classes, while high strange or gluon scores shift events towards the $H \rightarrow s\bar{s}$ and $H \rightarrow gg$ hypotheses. Missing-energy observables and m_{jj} dominantly drive the separation between $ZH(\nu\bar{\nu})$ and the $2f/4f$ backgrounds. Taken together, these studies show that the classifier performance is rooted in well-understood heavy- and light-flavor tagging information combined with global event kinematics, rather than in unphysical artefacts of the training.

3.4 Expected sensitivities and discussion

We now quantify the sensitivity to hadronic Higgs decays by using the event-level classifier outputs as one-dimensional discriminants, as outlined in Sec. 2.2. For each Higgs decay hypothesis, the corresponding XGBoost score is used to select a signal-enhanced region in which all other Higgs modes and the $2f/4f$ processes are treated as backgrounds. The threshold on the score is scanned, and for each working point the expected signal (S) and background (B) yields are computed. The statistical significance Z is then evaluated using Eq. (2.2), and the optimal working point is chosen as the threshold that maximizes Z .

Table 4. Selection efficiencies [%] for the four Higgs decay channels of interest. Each row shows the efficiency when the corresponding decay mode is treated as signal and all other Higgs modes and $2f/4f$ processes are treated as background.

Signal	Channel						
	$H \rightarrow b\bar{b}$	$H \rightarrow c\bar{c}$	$H \rightarrow gg$	$H \rightarrow s\bar{s}$	$H \rightarrow ZZ^*$	4f	2f
$H \rightarrow b\bar{b}$	53.89	2.73×10^{-3}	0.43	1.47×10^{-3}	8.39×10^{-4}	0.09	2.23×10^{-4}
$H \rightarrow c\bar{c}$	0.01	43.51	0.36	5.14×10^{-3}	5.77×10^{-4}	0.07	8.11×10^{-5}
$H \rightarrow gg$	0.16	0.39	50.17	1.76	4.19×10^{-4}	0.04	1.62×10^{-4}
$H \rightarrow s\bar{s}$	6.67×10^{-5}	0.05	0.75	44.68	1.65×10^{-4}	0.05	4.16×10^{-4}

Table 5. Event yields for the four Higgs decay channels of interest, normalized to 20 ab^{-1} . Each row corresponds to the case where that decay mode is treated as signal and all other modes are treated as background.

Signal	Channel						
	$H \rightarrow b\bar{b}$	$H \rightarrow c\bar{c}$	$H \rightarrow gg$	$H \rightarrow s\bar{s}$	$H \rightarrow ZZ^*$	4f	2f
$H \rightarrow b\bar{b}$	287924.98	0.73	347.03	0.003	0.06	7161.45	2414.79
$H \rightarrow c\bar{c}$	61.25	11747.07	283.73	0.01	0.04	5824.03	878.10
$H \rightarrow gg$	853.22	107.21	39836.00	3.52	0.030	3099.98	1756.21
$H \rightarrow s\bar{s}$	0.36	13.63	593.77	89.36	0.01	4059.50	101.05

Table 4 and Table 5 summarize the resulting selection efficiencies and event yields for the four Higgs decay channels of interest, using the `XGB_Combined` classifier and assuming 20 ab^{-1} . For illustration, when targeting $H \rightarrow s\bar{s}$ we obtain about 90 signal events with a background of about 4700 events, corresponding to a statistical significance of $Z \simeq 1.3\sigma$. Although this does not yet constitute an observation, it nevertheless provides a sensitivity estimate for $H \rightarrow s\bar{s}$ using a single channel $e^+e^- \rightarrow ZH \rightarrow \nu\bar{\nu}s\bar{s}$ at a lepton collider and provides a concrete benchmark for future improvements which will include more Z decay channels (eg. $Z \rightarrow \ell^+\ell^-, q\bar{q}$).

To assess the stability of the results and the benefit of combining different jet taggers, we repeat the full analysis chain for each of the four event-level classifiers: `XGB_PN`, `XGB_ParT`, `XGB_MIParT` and `XGB_Combined`. For every classifier, five statistically independent training runs are performed, yielding a distribution of projected precisions for each Higgs decay channel. The results are summarized in Fig. 7, where the bars indicate the mean precision and the error bars span the full range (maximum–minimum) observed across the five runs.

For $H \rightarrow b\bar{b}$ and $H \rightarrow c\bar{c}$, all four classifiers achieve similar sub-permille and percent-level precisions, respectively. The combination of the three jet taggers brings only marginal improvement, which is expected given the already high purity and strong kinematic separation of these modes. For $H \rightarrow gg$, the combined classifier provides a noticeable gain: the central precision improves and, more importantly, the spread among independent trainings is reduced, indicating that the ensemble is more robust against statistical fluctuations in the training process. In the most challenging $H \rightarrow s\bar{s}$ channel, the projected precision remains at the level of $\sim 78\%$, reflecting the limited signal statistics and the residual overlap with $H \rightarrow gg$ and $4f$ backgrounds. Nevertheless, the `XGB_Combined` classifier yields the best central value, and its entire variation band lies below those of the other three models, demonstrating that the multi-architecture combination is beneficial precisely where the problem is most difficult.

A direct comparison with previous CEPC and FCC-ee projections is given in Table 6. The ‘‘CEPC’’ column quotes the relative precisions on $\sigma(ZH) \times \text{Br}(H \rightarrow X)$ obtained in the CEPC Higgs benchmark study [37] for the $\nu\bar{\nu}H$ channel, rescaled to 20 ab^{-1} , while

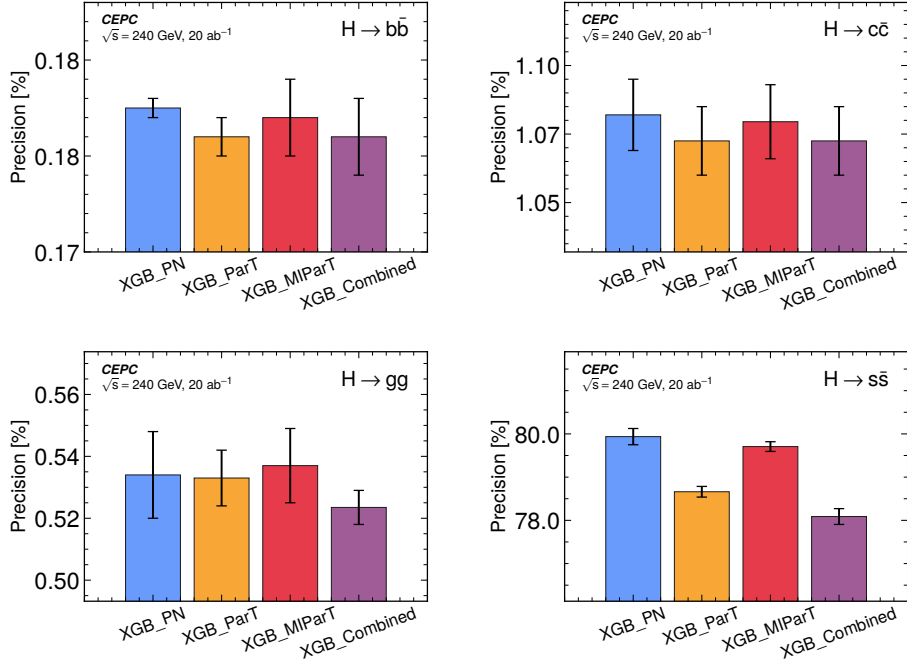


Figure 7. Relative precision on different Higgs decay channels for the four event-level classifiers: XGB_PN, XGB_ParT, XGB_MIParT, and XGB_Combined. For each classifier, 5 independent training runs are performed; the bars show the mean precision and the error bars indicate the full variation range (max–min) among the runs. Panels correspond to $H \rightarrow b\bar{b}$, $H \rightarrow c\bar{c}$, $H \rightarrow gg$, and $H \rightarrow s\bar{s}$, respectively.

Table 6. Comparison of relative measurement precision for various Higgs decay channels between the CEPC Higgs benchmark [37], FCC-ee [38] and this work, normalized to 20 ab^{-1} . The last column shows the relative improvement in precision with respect to the CEPC benchmark.

Channel	CEPC	FCC-ee	This work	Imp. vs CEPC
$Z \rightarrow \nu\bar{\nu}, H \rightarrow b\bar{b}$	0.20%	0.28%	0.18%	10%
$Z \rightarrow \nu\bar{\nu}, H \rightarrow c\bar{c}$	1.85%	1.95%	1.07%	42%
$Z \rightarrow \nu\bar{\nu}, H \rightarrow gg$	0.70%	0.78%	0.52%	26%
$Z \rightarrow \nu\bar{\nu}, H \rightarrow s\bar{s}$	—	117%	78%	—

the “FCC-ee” column shows the corresponding projections from the FCC-ee study [38]. The “This work” column gives the results from the XGB_Combined classifier in this study. For $H \rightarrow c\bar{c}$ the precision improves from 1.85% to 1.07%, corresponding to a relative gain of about 42%. For $H \rightarrow gg$ the precision improves from 0.70% to 0.52% (about 26% gain), and for $H \rightarrow b\bar{b}$ a modest but non-negligible improvement from 0.20% to 0.18% is observed. The $H \rightarrow s\bar{s}$ mode was not included in the CEPC benchmark study; our study provides a quantitative estimate, with a projected precision of about 78%. Relative to the

FCC-ee projections, the uncertainties are reduced by about 36% and 45% for $H \rightarrow b\bar{b}$ and $H \rightarrow c\bar{c}$, respectively, and by about 33% for both $H \rightarrow gg$ and $H \rightarrow s\bar{s}$. These quantitative differences with respect to the FCC-ee study should be interpreted with care, as they partly reflect different assumptions on detector performance and reconstruction, as well as the use of different jet-flavor tagging networks and event-level classification strategies in the respective analyses.

The improvements for $H \rightarrow c\bar{c}$ and $H \rightarrow gg$ demonstrate the impact of modern particle-level deep learning on Higgs measurements at future e^+e^- colliders. By directly exploiting the fine-grained jet substructure and combining multiple complementary taggers in a two-stage analysis, we achieve substantially better separation between quark and gluon jets and among different quark flavors than methods based solely on hand-crafted observables.

The $H \rightarrow s\bar{s}$ channel remains statistically limited in the baseline CEPC configuration considered here. However, the present analysis shows that even with 20 ab^{-1} it is possible to reach a sensitivity at the level of $Z \sim 1.3\sigma$. Future lepton colliders with higher luminosity, or combined analyses including additional Z decay modes beyond $Z \rightarrow \nu\bar{\nu}$, could further enhance the sensitivity and discovery potential. In addition, systematic uncertainties, such as those associated with jet energy scale, flavor-tagging calibration, and theoretical modeling of $2f/4f$ backgrounds, have not been included in the present study and will need to be assessed in more realistic scenarios. Nevertheless, the framework developed here is readily extendable: once experimental calibrations are available, the same two-stage strategy can incorporate data-driven constraints and systematic nuisance parameters in a global fit.

Previous work has explored an alternative “holistic” classification strategy [52], in which the full reconstructed event is fed to an event classifier realized using ParticleNet. When the comparison is restricted to the $\nu\nu H$ channel with $H \rightarrow b\bar{b}, c\bar{c}, gg, s\bar{s}$ as signal, the $2f$ and $4f$ backgrounds are omitted, the resulting statistical precisions are very similar to those obtained with our two-stage framework, providing a useful handle for validating jet-origin identification. A detailed numerical comparison and discussion are given in Appendix C. They further observed that using PYTHIA 8.313 instead of PYTHIA 6.4 improves the relative precision of the $H \rightarrow s\bar{s}$ final state by about 40%, in particular by producing a higher rate of K^\pm mesons, which in turn enhances the separation of s-jets. In the present study we deliberately employ PYTHIA 6.4 in order to remain aligned with the CEPC-TDR simulation setup, and our primary goal is to establish and validate the analysis strategy. The impact of updated generator configurations, such as PYTHIA 8.313, and their inclusion in a full combined analysis over all Z decay channels will be investigated in future work.

4 Conclusions

In this paper we have studied the prospects for measuring hadronic Higgs decays at a future high-luminosity e^+e^- Higgs factory, using the CEPC as a concrete benchmark. Focusing on $e^+e^- \rightarrow ZH$ with $Z \rightarrow \nu\bar{\nu}$ and $H \rightarrow q\bar{q}, gg$, we developed a unified two-stage analysis framework that combines three state-of-the-art particle-level jet taggers, ParticleNet, Particle Transformer (ParT) and More-Interaction Particle Transformer (MIParT), with

an event-level XGBoost classifier. This approach efficiently exploits both jet substructure and global event kinematics to separate $H \rightarrow b\bar{b}$, $H \rightarrow c\bar{c}$, $H \rightarrow s\bar{s}$ and $H \rightarrow gg$ from the dominant $2f$ and $4f$ backgrounds.

Assuming an integrated luminosity of 20 ab^{-1} at $\sqrt{s} = 240 \text{ GeV}$, we obtain projected relative uncertainties on $\sigma(ZH) \times \text{Br}(H \rightarrow X)$ of 0.18% for $X = b\bar{b}$, 1.07% for $c\bar{c}$, 0.52% for gg and 78% for $s\bar{s}$ in the $Z \rightarrow \nu\bar{\nu}$ channel. Compared with the CEPC Higgs benchmark study, the precisions for $H \rightarrow c\bar{c}$ and $H \rightarrow gg$ are improved by about 42% and 26%, respectively, while $H \rightarrow b\bar{b}$ improves modestly from 0.20% to 0.18%. For $H \rightarrow s\bar{s}$ we provide a quantitative sensitivity estimate at a lepton collider, corresponding to a statistical significance of about 1.3σ and establishing a concrete benchmark for future probes of the strange-quark Yukawa coupling.

Although the present study considers only statistical uncertainties and a single Z decay mode, it already illustrates the potential of particle-level deep learning for Higgs physics at lepton colliders. A more complete assessment will require the inclusion of experimental and theoretical systematics, detailed detector calibrations (in particular for jet energy scale and flavor tagging), and the combination of multiple ZH final states such as $Z \rightarrow \ell^+\ell^-$ and $Z \rightarrow q\bar{q}$. Higher integrated luminosities, or staged running at different center-of-mass energies, would further enhance the reach for rare decays such as $H \rightarrow s\bar{s}$.

The sensitivity of $H \rightarrow ss$ measurements can be enhanced via three key avenues: improved detector performance, advanced jet origin identification algorithms, and rigorously validated hadronization models. At the current analysis threshold, the dominant backgrounds to $H \rightarrow ss$ are Standard Model four-fermion processes with identical parton color configurations and $H \rightarrow gg$ processes. The former background can be suppressed by optimizing the reconstruction of the total invariant mass and recoil mass of the hadronic system—an objective aligned with the emerging concept of one-to-one correspondence detectors. Reducing contamination from $H \rightarrow gg$ processes, by contrast, relies on enhanced discrimination between gluon-initiated and strange-quark-initiated jets; as demonstrated in Ref. [52], accurate modeling and validation of hadronization frameworks are critical to this end. It is also worth noting that $H \rightarrow ss$ measurements remain hampered by inherent theoretical challenges [53], which necessitate targeted follow-up studies.

Finally, while our numerical results are obtained for the CEPC reference design, the analysis strategy developed here is readily applicable to other proposed Higgs factories, including FCC-ee and ILC, by updating the detector response and luminosity assumptions. Together with the gains demonstrated for $H \rightarrow c\bar{c}$ and $H \rightarrow gg$ and a quantitative projection for $H \rightarrow s\bar{s}$, this work highlights the important role that advanced machine-learning techniques can play in fully mapping out the flavor structure of the Higgs sector at future lepton colliders.

Acknowledgments

We thank Chongqiao Li and Kaili Zhang for useful discussions and comments. This work was supported by the National Natural Science Foundation of China under Grant No.

W2441004. The work of Kun Wang was supported by the Open Project of the Shanghai Key Laboratory for Particle Physics and Cosmology under Grant No. 22DZ2229013-3.

A Preselection kinematics

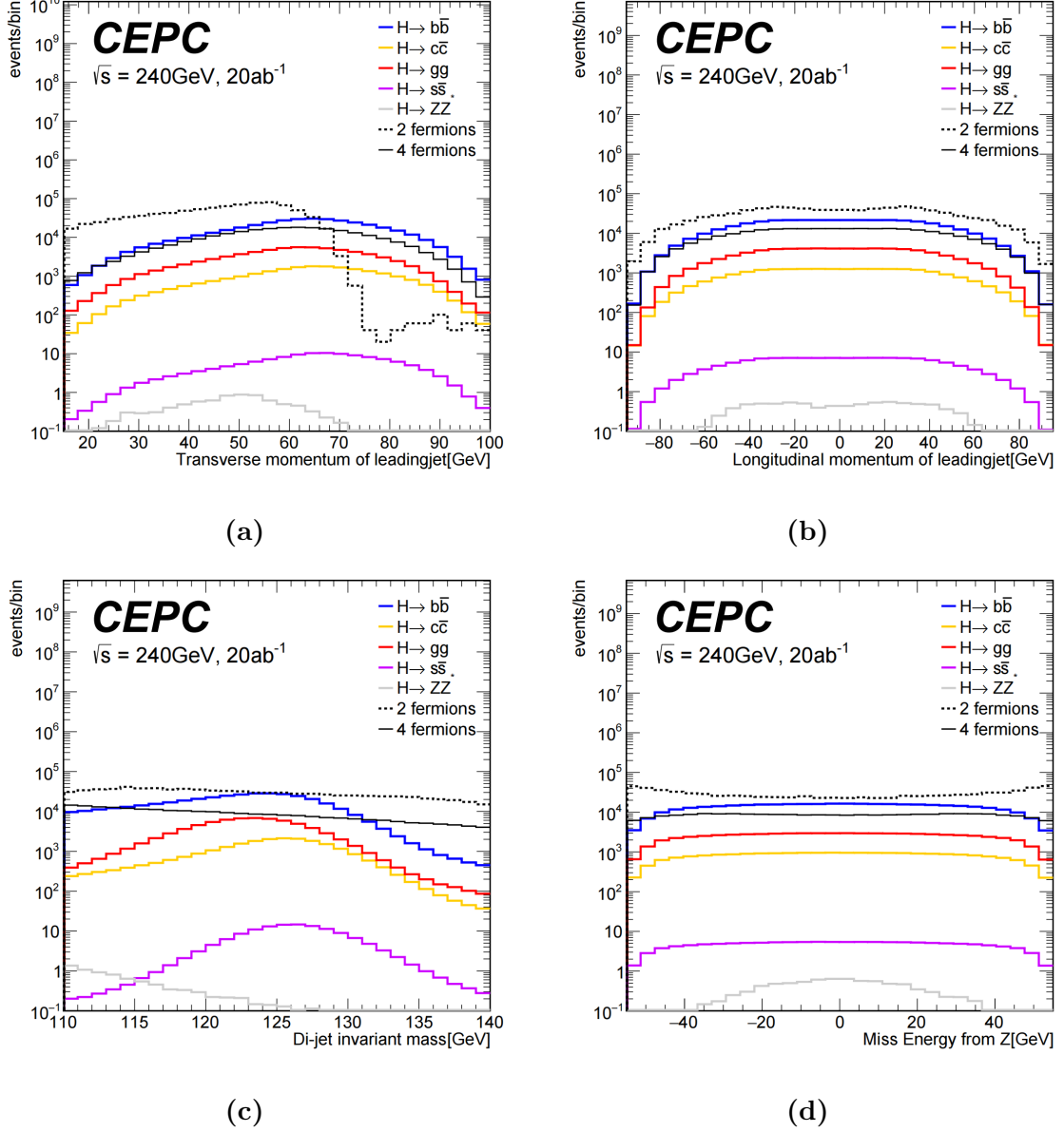


Figure 8. Distributions of the preselection observables used as inputs to the event-level multivariate analysis: (a) transverse momentum $p_T(j)$ and (b) longitudinal momentum $p_z(j)$ of the leading jet, (c) invariant mass m_{jj} of the dijet system, and (d) longitudinal component of the missing energy $E_{z,\text{miss}}$. All distributions are shown after event-quality selections and normalised to 20ab^{-1} .

As discussed in Sec. 2.2, a loose preselection is applied before training the event-level XGBoost classifiers. The aim of this step is twofold: (i) to enhance the $ZH(\nu\bar{\nu})$ topology

and suppress the large inclusive $2f$ and $4f$ backgrounds, and (ii) to stabilise the kinematic phase space over which the multivariate classifier is trained, so that it can focus on finer differences related to jet flavour. The preselection uses four global observables: the transverse (p_T) and longitudinal (p_z) momenta of the leading jet, the invariant mass of the dijet system m_{jj} , and the longitudinal component of the missing energy $E_{z,\text{miss}}$. Figures 8(a)–(d) show the distributions of these variables for the main signal and background processes, after basic event-quality requirements and normalised to an integrated luminosity of 20 ab^{-1} .

The leading-jet transverse momentum $p_T(j)$, shown in Fig. 8(a), reflects the recoil of the Higgs boson against the $Z \rightarrow \nu\bar{\nu}$ system. In $e^+e^- \rightarrow ZH$ at $\sqrt{s} = 240 \text{ GeV}$ the Higgs is produced close to threshold, so that its decay products carry typical transverse momenta of order $m_H/2$. Consequently, all hadronic Higgs decay modes peak in a relatively narrow range around $p_T(j) \sim 50\text{--}70 \text{ GeV}$. In contrast, the $2f$ background $e^+e^- \rightarrow q\bar{q}$ originates from γ^*/Z exchange and exhibits a much broader spectrum, extending to both lower and higher p_T values, while the $4f$ processes populate mainly the lower- p_T region. Requiring $15 < p_T(j) < 100 \text{ GeV}$ therefore retains the bulk of the Higgs signal while efficiently rejecting very soft and very hard $2f/4f$ topologies that are kinematically incompatible with ZH .

The longitudinal momentum $p_z(j)$ of the leading jet, displayed in Fig. 8(b), encodes the polar-angle distribution of the event. Since the Higgs boson is predominantly produced centrally in $e^+e^- \rightarrow ZH$, the jets from its decay tend to be central as well, resulting in a fairly flat distribution in p_z within a limited range. By contrast, the $2f$ background is strongly peaked at forward angles, leading to an enhanced rate at large $|p_z(j)|$. The symmetric requirement $|p_z(j)| < 95 \text{ GeV}$ exploits this difference, suppressing a large fraction of the forward-peaked $2f$ events while leaving the ZH signal essentially unaffected.

Fig. 8(c) shows the invariant mass of the dijet system, m_{jj} . For genuine ZH events the two reconstructed jets originate from the Higgs decay and therefore cluster around the Higgs boson mass, with a resolution of a few GeV determined by the detector and reconstruction performance. This leads to the characteristic peak near $m_{jj} \simeq 125 \text{ GeV}$ for all hadronic Higgs decay modes. In contrast, the $2f$ background forms a broad continuum in m_{jj} , while the $4f$ processes (including $\nu\bar{\nu}q\bar{q}$) exhibit a wider distribution reflecting different intermediate boson masses and off-shell configurations. The mass window $110 < m_{jj} < 140 \text{ GeV}$ is therefore an efficient handle to enhance the Higgs contribution and is also used as an input feature for the multivariate analysis.

Finally, Fig. 8(d) presents the distribution of the longitudinal component of the missing energy, $E_{z,\text{miss}}$, which is reconstructed from the vector sum of all visible final-state particles. In signal events, the missing momentum is dominated by the $Z \rightarrow \nu\bar{\nu}$ decay and is thus correlated with the recoil of the Higgs system, leading to a relatively broad distribution in $E_{z,\text{miss}}$ that is symmetric around zero. For the $2f$ background there is no genuine source of missing energy; the small apparent $E_{z,\text{miss}}$ arises from detector resolution and acceptance losses and is therefore concentrated near zero. The $4f$ background lies in between these two extremes. Imposing $|E_{z,\text{miss}}| < 55 \text{ GeV}$ suppresses extreme configurations in which the apparent missing momentum is aligned with the beam direction, which are predominantly due to background or poorly reconstructed events.

Taken together, these four observables capture the essential kinematic features of the $ZH(\nu\bar{\nu})$ topology: a centrally produced Higgs boson decaying to two jets with an invariant mass near m_H and recoiling against genuine missing energy. The preselection cuts quoted in Sec. 2.2 retain about 80% of the Higgs signal while rejecting more than 97% of the inclusive $2f$ and $4f$ backgrounds. At the same time, the full distributions shown in Fig. 8 are used as inputs to the XGBoost classifier, allowing the multivariate analysis to exploit the residual shape differences beyond the simple rectangular cuts.

B Event-level classifier details

In this appendix we provide additional information on the training of the XGBoost event-level classifiers and discuss, from a physics perspective, which input variables drive the separation between signal and background hypotheses.

B.1 XGBoost setup and training strategy

The event classification is performed with gradient-boosted decision trees as implemented in XGBOOST [36]. We employ a multi-class setup in which six classes are distinguished simultaneously: $H \rightarrow b\bar{b}$, $H \rightarrow c\bar{c}$, $H \rightarrow s\bar{s}$, $H \rightarrow gg$, and the $2f$ and $4f$ backgrounds. The classifier output is therefore a six-component probability vector for each event, and the score associated with a particular signal hypothesis is used as the one-dimensional discriminant in Sec. 3.4.

The main hyperparameters are chosen so as to balance model complexity, training stability and robustness against overfitting:

- The maximum depth of each decision tree is set to `max_depth = 3`.
- The learning rate is scheduled in three stages: $\eta = 0.1$ for the first 600 boosting rounds, $\eta = 0.05$ for rounds 601–800, and $\eta = 0.01$ for the last 200 rounds, with a total of `n_estimators = 1000` trees.
- To introduce additional regularisation and decorrelation among trees we use row and column subsampling, `subsample = 0.8` and `colsample_bytree = 0.8`, respectively.
- The objective function is the multiclass logarithmic loss (`multi:softprob` in XGBOOST), and the default ℓ_2 regularisation parameters are retained as further stabilisers.

B.2 Physics interpretation

The XGBoost classifiers take as input both global event observables and the flavor probabilities predicted by the three jet taggers (PN, ParT and MIParT) for the two Higgs-candidate jets (cf. Table 3). To understand which information the classifier exploits most strongly, we study the relative importance of each input feature using two complementary measures:

1. The total gain attributed to a feature, summed over all decision trees in the ensemble, as feature importance, which quantifies how much this feature contributes to reducing the training loss.

2. SHapley Additive exPlanations (SHAP) values [50], which characterise, event by event, how much each input variable pushes the classifier output towards or away from a specific class. In the multi-class setting used here, a separate SHAP value is computed for each class.

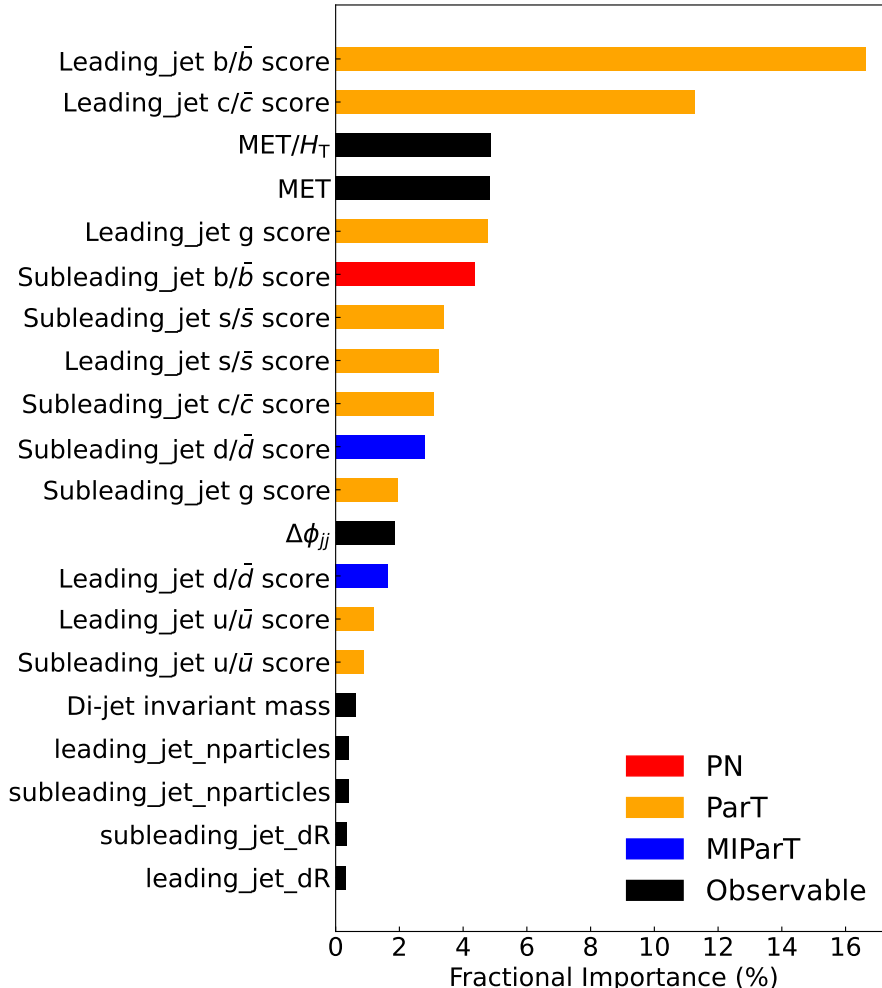


Figure 9. Top 20 most important input variables for the `XGB_Combined` classifier, ranked by their total gain fraction in the boosted decision-tree ensemble. Entries are colour-coded according to their origin: PN, ParT, MIParT, or high-level kinematic observables.

Global feature importance from gain

Fig. 9 shows the 20 most important input features for the `XGB_Combined` classifier, ranked according to their total gain. Each entry is colour-coded according to its origin: PN, ParT, MIParT or a high-level observable. Several physics-driven patterns are immediately visible.

We can see that the jet flavor scores are clearly dominant in the ranking. In particular, the ParT scores for the leading-jet b and c hypotheses are the two most important features. This is physically expected: heavy-flavor tagging provides the primary handle to separate

$H \rightarrow b\bar{b}$ and $H \rightarrow c\bar{c}$ from the light-flavor Higgs decays and from the $2f/4f$ backgrounds. The corresponding scores for the subleading jet, as well as the strange and gluon probabilities for both jets, also appear high in the list. They are essential for distinguishing $H \rightarrow s\bar{s}$ and $H \rightarrow gg$ from each other and from the inclusive light-quark background. The fact that PN and MIParT scores for the same flavor categories also enter among the top-ranked variables demonstrates that the three jet taggers provide partially complementary information: XGBoost learns to assign different weights to their outputs depending on the flavor and on whether the jet is leading or subleading in p_T .

Among the non-jet-flavor observables, the missing transverse energy and the ratio of missing to visible transverse momentum are the most important. This reflects the crucial role of the $Z \rightarrow \nu\bar{\nu}$ topology in separating signal from the $2f$ background, which has no genuine neutrinos and thus only small, resolution-driven missing energy. Other kinematic variables such as the transverse momentum of the leading jet and the azimuthal separation $\Delta\phi_{jj}$ between the two jets also contribute: they are sensitive to differences in the recoil kinematics and event shapes between ZH production and generic $2f/4f$ processes.

Per-class SHAP analysis

While the gain ranking tells us which features matter on average, it does not show how a given variable affects the classification of individual events. For that purpose we use SHAP values [50], which provide a local, event-by-event decomposition of the classifier output.

For a fixed output class c (e.g., $H \rightarrow b\bar{b}$ or $2f$) and a given event x , the SHAP value of a feature x_i represents its contribution to the classifier score $f_c(x)$, relative to the average score $\langle f_c \rangle$ over the event sample. In the XGBoost implementation used here, the classifier assigns a continuous score to each class, and the SHAP values approximately sum to the difference between this score and its average:

$$f_c(x) - \langle f_c \rangle \simeq \sum_i \text{SHAP}_{c,i}(x). \quad (\text{B.1})$$

where the sum runs over all input features x_i in the event.

A positive SHAP value for class c indicates that, given the observed value of this feature, the classifier is pushed to favour class c more than it would for a typical event; a negative value means that the feature pushes the prediction away from that class. The magnitude of the SHAP value indicates the strength of this effect.

Fig. 10 shows SHAP “summary” plots for each of the six output classes. In each panel, the vertical axis lists the 10 most important variables for that class. Every point corresponds to one event in the test sample. The horizontal position of a point is the SHAP value for that event and feature, so the spread along the x -axis indicates how strongly that variable can move events towards or away from the class under consideration. The colour encodes the value of the feature itself: red points correspond to events where this feature takes a relatively large value (for example, a high b -tag score or a large MET), while blue points correspond to small values. Regions where many points accumulate indicate that a given combination of feature value and SHAP impact is common in the sample; sparser regions typically correspond to rarer, more extreme events.

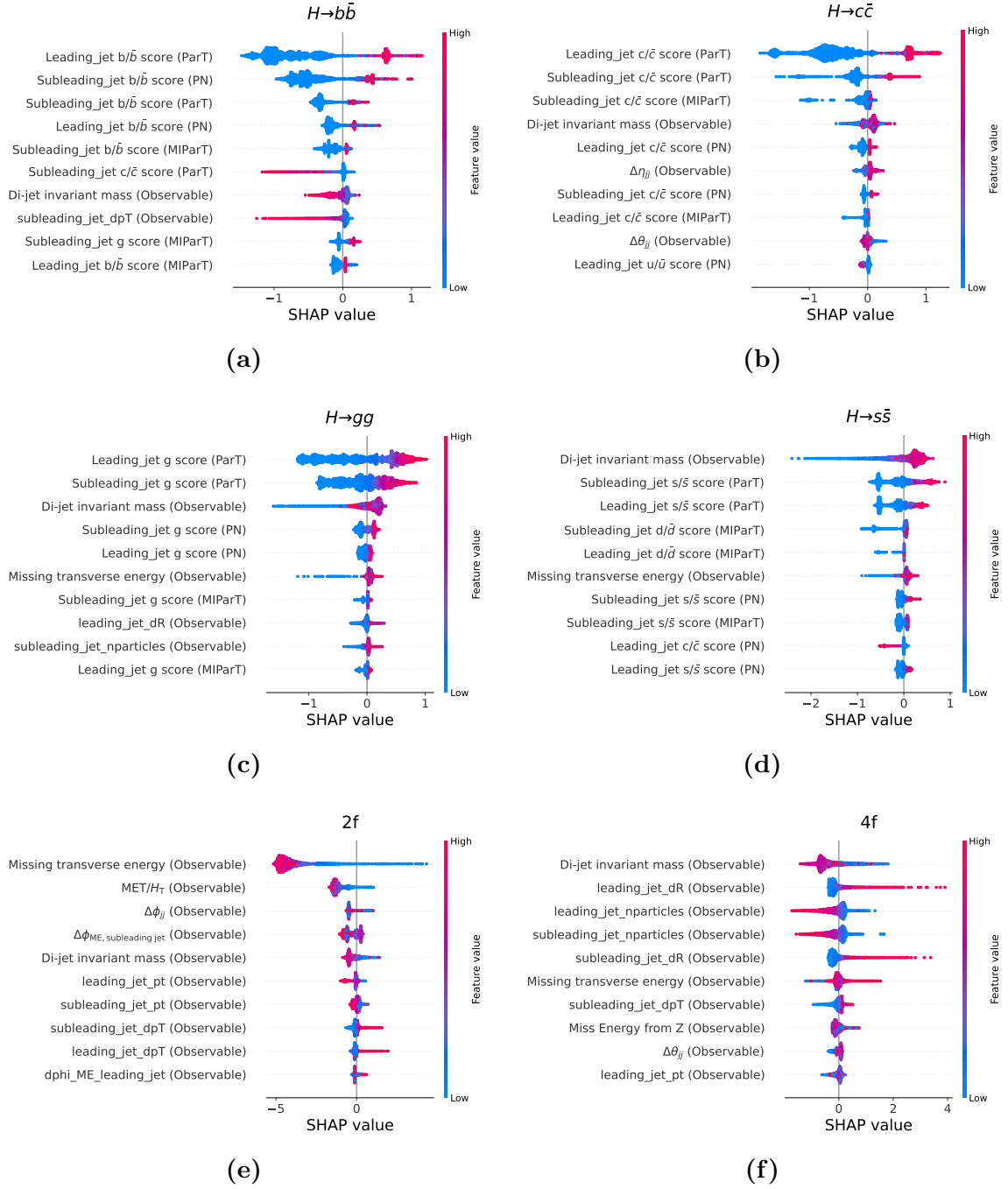


Figure 10. SHAP summary plots for the event-level XGB_Combined classifier, showing the ten most influential variables for each of the six output classes. In each panel, every point corresponds to a single event; the horizontal axis gives the SHAP value for that feature and class, while the colour encodes the feature value (from low in blue to high in red). Panels correspond to (a) $H \rightarrow b\bar{b}$, (b) $H \rightarrow c\bar{c}$, (c) $H \rightarrow gg$, (d) $H \rightarrow s\bar{s}$, (e) $2f$, (f) $4f$.

With this in mind, the structure of the SHAP plots is readily interpreted in physical terms.

- For the $H \rightarrow b\bar{b}$ and $H \rightarrow c\bar{c}$ classes, shown in panels (a) and (b), the leading b - and c -jet scores show red points (high flavor score) predominantly at positive SHAP values and blue points (low score) at negative SHAP values. This means that jets with a large b - or c -tagging probability systematically push the classifier towards the corresponding Higgs decay hypothesis, while jets with small scores make the event look less like $H \rightarrow b\bar{b}$ or $H \rightarrow c\bar{c}$. This behaviour is exactly what one expects from a physically sensible heavy flavor tagger.
- For the $H \rightarrow gg$ and $H \rightarrow s\bar{s}$ classes, shown in panels (c) and (d), the most important variables are the gluon and strange scores of both jets and the dijet invariant mass m_{jj} . Large gluon (strange) scores favour the $H \rightarrow gg$ ($H \rightarrow s\bar{s}$) hypothesis, while small scores have the opposite effect. The m_{jj} distribution shows that events with a dijet mass close to the Higgs mass peak tend to have positive SHAP values for these classes, whereas events far away from the peak tend to be pushed towards the background hypotheses. The fact that both red and blue points appear on either side of the vertical axis reflects the presence of correlations: for example, an event with a moderately high strange score may still be classified as background if other features (such as MET or jet kinematics) look incompatible with a $ZH(\nu\bar{\nu})$ topology.
- For the $2f$ and $4f$ background classes, shown in panels (e) and (f), the most influential variables are global observables such as MET, m_{jj} , jet MET angular correlations and jet shape variables. Here the SHAP plots show that small MET values and dijet masses away from m_H tend to yield positive SHAP values for the $2f$ class, indicating that such events look more like generic $e^+e^- \rightarrow q\bar{q}$ production than like a signal ZH event. In contrast, large MET and a Higgs-like m_{jj} value tend to suppress the $2f$ score and enhance the Higgs decay classes, as expected.

Overall, the SHAP analysis confirms and refines the picture obtained from the gain ranking: the classifier relies mainly on heavy and light flavor tagging information to distinguish between different Higgs decay modes, while global kinematic observables associated with the $ZH(\nu\bar{\nu})$ topology are used to separate signal from the inclusive $2f/4f$ backgrounds. The decision boundaries learned by the model are therefore well aligned with standard physics intuition.

Performance studies guided by interpretability

The interpretability studies presented above naturally motivate targeted performance cross-checks. Here we investigate how the classifier performance changes when the input feature set is systematically restricted, guided by the global feature-importance and per-class SHAP analyses. We consider two complementary variations of the input configuration:

- **Impact of individual jet taggers.** To probe the relative importance of the three jet taggers, we retrain the event-level classifier using only the ParT, MIParT, or

PN flavor scores as jet inputs, while keeping the same set of event-level kinematic observables. The resulting precisions on $\sigma(ZH) \times \text{Br}(H \rightarrow X)$ are summarised in Table 7. Using only the ParT scores already reproduces nearly the full performance of the `XGB_Combined` configuration, consistent with the dominance of ParT variables observed in Fig. 9. Including PN and MIParT scores leads to small but non-negligible improvements, particularly for the $H \rightarrow gg$ and $H \rightarrow s\bar{s}$ channels, and reduces the spread among independent training runs. This indicates that the three taggers capture partially complementary aspects of the jet substructure.

- **Reduced-input study based on top features.** To assess how much of the classification performance can be retained with a smaller and more interpretable input space, we construct a reduced-input classifier, denoted `XGB_Topfeatures`. The input variables of this classifier are selected in two steps. First, we retain the ten most important features according to the global feature-importance ranking obtained from the full `XGB_Combined` model. Second, for each output class of the multi-class classifier, we add the five features with the largest absolute SHAP values in the corresponding class-specific SHAP summary. After removing duplicates between classes and with the globally selected features, the final input set contains 26 variables, listed in Table 8.. The `XGB_Topfeatures` classifier is trained with the same architecture and training configuration as `XGB_Combined`. The expected precisions obtained with `XGB_Topfeatures`, reported in Table 7, are comparable to those of the full-feature configuration. This indicates that a large fraction of the discriminating power of the original classifier is already captured by a relatively small subset of physically interpretable features.

Table 7. Comparison between the full XGBoost configuration (`XGB_Combined`) and reduced configurations in which the jet inputs are restricted to only the ParT, MIParT or PN scores, while retaining the full set of event-level kinematic observables. Also shown is a reduced-input setup (`XGB_Topfeatures`) guided by the feature importance and SHAP analyses, in which the overall input set is restricted to a compact subset of the most relevant variables.

Channel	<code>XGB_Combined</code>	<code>XGB_ParT</code>	<code>XGB_MIParT</code>	<code>XGB_PN</code>	<code>XGB_Topfeatures</code>
$Z \rightarrow \nu\bar{\nu}, H \rightarrow b\bar{b}$	0.18%	0.18%	0.18%	0.18%	0.18%
$Z \rightarrow \nu\bar{\nu}, H \rightarrow c\bar{c}$	1.07%	1.07%	1.08%	1.08%	1.10%
$Z \rightarrow \nu\bar{\nu}, H \rightarrow gg$	0.52%	0.53%	0.54%	0.53%	0.55%
$Z \rightarrow \nu\bar{\nu}, H \rightarrow s\bar{s}$	78%	79%	80%	80%	82%

C Comparison with holistic event-level classification

Reference [52] has proposed a ‘holistic’ strategy for classifying hadronic Higgs decays at lepton colliders. In that approach, the entire reconstructed event is treated as a single particle cloud and passed to an event-level ParticleNet classifier. All reconstructed particles and their low-level features (kinematics, particle identification, track information, etc.)

Table 8. List of input variables used in the reduced-input XGBoost classifier (`XGB_Topfeatures`). Event-level and jet-level kinematic quantities are shown first, followed by jet-flavour tagging scores from the ParT, PN and MIParT taggers for the leading and subleading jets. Here and in the following, j_1 and j_2 denote the leading and subleading jets in p_T , respectively.

Feature(s)	Description
<i>Event- and jet-level kinematics</i>	
MET	Magnitude of the missing transverse energy
MET/ H_T	MET to H_T ratio
m_{jj}	Invariant mass of the dijet system
$\Delta\phi_{jj}$	$\Delta\phi$ between the two jets
$\Delta\phi(j_2, \text{MET})$	$\Delta\phi$ between subleading jet and MET
$\Delta R(j_1, j_2)$	Angular distance between the two jets
$n_{\text{part}}(j_1), n_{\text{part}}(j_2)$	Leading/subleading jet particle multiplicities
<i>Jet-flavour tagging scores</i>	
ParT (leading jet): $\bar{b}, \bar{c}, \bar{s}, s, g$	ParT jet flavour scores for leading jet
ParT (subleading jet): $\bar{b}, b, \bar{c}, c, \bar{s}, s, g$	ParT jet flavour scores for subleading jet
PN (leading jet): \bar{b}, g	ParticleNet jet flavour scores for leading jet
PN (subleading jet): b, g	ParticleNet jet flavour scores for subleading jet
MIParT (subleading jet): c	MIParT jet flavour scores for subleading jet

enter directly as inputs, without an explicit intermediate jet reconstruction or jet-by-jet flavor tagging step. The network is therefore responsible for learning both the internal jet substructure and the global event topology in a single stage and produces, for each event, likelihoods for a set of signal hypotheses.

By contrast, the strategy developed in this work decomposes the problem into two physically motivated levels: (i) jet-level flavor classification using ParticleNet, ParT and MIParT, and (ii) event-level classification using XGBoost, which takes as inputs both global kinematic observables and the jet-flavor probabilities from the three taggers. This modular structure explicitly separates microscopic jet-substructure information from global event kinematics, which is advantageous for interpretability and for the eventual treatment of systematic uncertainties.

To compare the physics reach of the two strategies in a controlled way, we reproduce, as closely as possible, the setup of Ref. [52]. In particular:

- We restrict the comparison to the $e^+e^- \rightarrow ZH$ channel with $Z \rightarrow \nu\bar{\nu}$;
- We consider only the four hadronic Higgs decay modes $H \rightarrow b\bar{b}, c\bar{c}, gg$ and $s\bar{s}$, treating them as mutually exclusive classes; and
- We do not include the $2f$ and $4f$ backgrounds in this comparison, in order to focus on the relative separation power among the different Higgs decay modes themselves.

Using exactly the same significance definition and optimisation procedure as in Sec. 3.4, we determine the expected relative precision on $\sigma(ZH) \times \text{Br}(H \rightarrow X)$ for each channel in our two-stage framework and normalise the results to an integrated luminosity of 20 ab^{-1} . The corresponding numbers from the holistic ParticleNet study are taken from Ref. [52]. The comparison is summarised in Table 9.

Table 9. Comparison of the relative statistical precision on $\sigma(ZH) \times \text{Br}(H \rightarrow X)$ in the $Z \rightarrow \nu\bar{\nu}$ channel between this work (two-stage classification) and the holistic ParticleNet event-level classifier of Ref. [52]. Only the four Higgs decay modes $H \rightarrow b\bar{b}$, $c\bar{c}$, gg and $s\bar{s}$ are considered, without including the $2f$ and $4f$ backgrounds. All values are normalised to an integrated luminosity of 20 ab^{-1} .

Channel	This work	Holistic [52]
$Z \rightarrow \nu\bar{\nu}, H \rightarrow b\bar{b}$	0.17%	0.14%
$Z \rightarrow \nu\bar{\nu}, H \rightarrow c\bar{c}$	0.77%	0.72%
$Z \rightarrow \nu\bar{\nu}, H \rightarrow gg$	0.47%	0.46%
$Z \rightarrow \nu\bar{\nu}, H \rightarrow s\bar{s}$	29%	29%

The two approaches yield very similar sensitivities. For the high-rate channels $H \rightarrow b\bar{b}$, $c\bar{c}$ and gg , the relative precisions agree within a few tenths of a per mille to a few tenths of a percent, well below the level at which other theoretical or experimental systematics are expected to enter. In the statistically more challenging $H \rightarrow s\bar{s}$ channel, both methods reach a relative precision of about 29% under the idealised assumptions of this comparison. These results indicate that, at least in this simplified setup, the explicit use of jet reconstruction and dedicated jet-flavor taggers does not lead to any loss of information compared to a fully holistic treatment of the event; both strategies appear to saturate the discriminating power available in the simulated samples.

However, it is important to emphasise the conceptual differences between the two approaches, which become particularly relevant once systematic effects and more complex final states are considered:

- **Modularity and calibration.** In the two-stage framework, the jet-level taggers and the event-level classifier are separate components. The jet taggers can in principle be calibrated and validated using control samples enriched in specific flavours (e.g. $Z \rightarrow b\bar{b}$, $Z \rightarrow c\bar{c}$, light-flavor and gluon jets), while the event-level XGBoost can be retrained or fine-tuned using these calibrated inputs. This modularity is advantageous for controlling systematic uncertainties in a real experiment. In a holistic network, the flavor and topology information are entangled in a single, monolithic model, making it more challenging to isolate and correct potential mismodellings in specific physics components.
- **Reusability and flexibility.** Once trained, jet-level taggers can be reused across many different analyses and channels (e.g. other Higgs production modes or Z -pole measurements), with only the event-level classifier needing to be adapted to a new

topology. A holistic event-level network would typically have to be retrained for each new physics channel or detector configuration, which is computationally more demanding and less transparent.

- **Interpretability.** The two-stage method provides a clear physics picture of how different ingredients contribute: heavy-flavor scores drive the separation of $H \rightarrow b\bar{b}$ and $H \rightarrow c\bar{c}$, strange and gluon scores control the $H \rightarrow s\bar{s}$ versus $H \rightarrow gg$ discrimination, and global kinematics (such as missing energy and jet angular correlations) distinguish $ZH(\nu\bar{\nu})$ from generic $2f/4f$ backgrounds. In a holistic model this decomposition is implicit and must be inferred a posteriori, e.g. via saliency maps, which can be more difficult to relate to specific experimental systematics.

In summary, the quantitative comparison in Table 9 shows that our two-stage jet-plus-event classifier achieves a statistical performance that is fully comparable to that of the holistic ParticleNet approach under the same simplified benchmark. At the same time, the modular structure of the two-stage strategy provides practical advantages for calibration, systematic-uncertainty control and reuse across channels, which are essential considerations for precision Higgs measurements at future lepton colliders.

References

- [1] ATLAS Collaboration, *A detailed map of higgs boson interactions by the atlas experiment ten years after the discovery*, *Nature* **607** (2022) 52.
- [2] CMS Collaboration, *A portrait of the higgs boson by the cms experiment ten years after the discovery*, *Nature* **607** (2022) 60.
- [3] S.F. Novaes, *Standard model: An Introduction*, in *10th Jorge Andre Swieca Summer School: Particle and Fields*, pp. 5–102, 1, 1999 [[hep-ph/0001283](#)].
- [4] P.W. Higgs, *Broken symmetries, massless particles and gauge fields*, *Phys. Lett.* **12** (1964) 132.
- [5] F. Englert and R. Brout, *Broken Symmetry and the Mass of Gauge Vector Mesons*, *Phys. Rev. Lett.* **13** (1964) 321.
- [6] G.S. Guralnik, C.R. Hagen and T.W.B. Kibble, *Global Conservation Laws and Massless Particles*, *Phys. Rev. Lett.* **13** (1964) 585.
- [7] T.W.B. Kibble, *Symmetry breaking in nonAbelian gauge theories*, *Phys. Rev.* **155** (1967) 1554.
- [8] ATLAS Collaboration, *Measurements of Higgs boson production and couplings in diboson final states with the ATLAS detector at the LHC*, *Phys. Lett. B* **726** (2013) 88 [[1307.1427](#)].
- [9] ATLAS Collaboration, *Observation and measurement of Higgs boson decays to WW^* with the ATLAS detector*, *Phys. Rev. D* **92** (2015) 012006 [[1412.2641](#)].
- [10] CMS Collaboration, *Measurements of higgs boson properties in the diphoton decay channel in proton-proton collisions at $\sqrt{s} = 13$ tev*, *Journal of High Energy Physics* **2018** (2018) .
- [11] CMS Collaboration, *Observation of Higgs boson decay to bottom quarks*, Tech. Rep. [CMS-PAS-HIG-18-016](#), CERN, Geneva (2018).
- [12] ATLAS Collaboration, *Observation of $H \rightarrow b\bar{b}$ decays and VH production with the ATLAS detector*, *Phys. Lett. B* **786** (2018) 59 [[1808.08238](#)].
- [13] CMS Collaboration, *Observation of the higgs boson decay to a pair of τ leptons with the cms detector*, *Physics Letters B* **779** (2018) 283–316.
- [14] ATLAS Collaboration, *Cross-section measurements of the Higgs boson decaying into a pair of τ -leptons in proton-proton collisions at $\sqrt{s} = 13$ TeV with the ATLAS detector*, *Phys. Rev. D* **99** (2019) 072001 [[1811.08856](#)].
- [15] ATLAS Collaboration, *Measurements of WH and ZH production with Higgs boson decays into bottom quarks and direct constraints on the charm Yukawa coupling in 13 TeV pp collisions with the ATLAS detector*, *JHEP* **04** (2025) 075 [[2410.19611](#)].
- [16] ATLAS collaboration, *Evidence for the Dimuon Decay of the Higgs Boson in pp Collisions with the ATLAS Detector*, *Phys. Rev. Lett.* **135** (2025) 231802 [[2507.03595](#)].
- [17] CMS collaboration, *Evidence for Higgs boson decay to a pair of muons*, *JHEP* **01** (2021) 148 [[2009.04363](#)].
- [18] P. Skands, *Introduction to QCD*, in *Theoretical Advanced Study Institute in Elementary Particle Physics: Searching for New Physics at Small and Large Scales*, pp. 341–420, 2013, DOI [[1207.2389](#)].

- [19] G. D’Ambrosio, G.F. Giudice, G. Isidori and A. Strumia, *Minimal flavor violation: An Effective field theory approach*, *Nucl. Phys. B* **645** (2002) 155 [[hep-ph/0207036](#)].
- [20] G.C. Branco, P.M. Ferreira, L. Lavoura, M.N. Rebelo, M. Sher and J.P. Silva, *Theory and phenomenology of two-Higgs-doublet models*, *Phys. Rept.* **516** (2012) 1 [[1106.0034](#)].
- [21] M. Redi and A. Weiler, *Flavor and CP Invariant Composite Higgs Models*, *JHEP* **11** (2011) 108 [[1106.6357](#)].
- [22] R. Harnik, J. Kopp and J. Zupan, *Flavor Violating Higgs Decays*, *JHEP* **03** (2013) 026 [[1209.1397](#)].
- [23] CEPC Study Group, *CEPC Conceptual Design Report: Volume 1 - Accelerator*, [1809.00285](#).
- [24] CEPC Study Group, *CEPC Conceptual Design Report: Volume 2 - Physics & Detector*, [1811.10545](#).
- [25] CEPC Study Group, *CEPC Technical Design Report: Accelerator, Radiation Detection Technology and Methods* **8** (2024) 1 [[2312.14363](#)].
- [26] CEPC Study Group, *CEPC Technical Design Report - Reference Detector*, [2510.05260](#).
- [27] I. Agapov et al., *Future Circular Lepton Collider FCC-ee: Overview and Status*, in *Snowmass 2021*, **3**, 2022 [[2203.08310](#)].
- [28] B. BARISH and J.E. BRAU, *The international linear collider*, *International Journal of Modern Physics A* **28** (2013) 1330039.
- [29] ATLAS collaboration, *Transforming jet flavour tagging at ATLAS*, [2505.19689](#).
- [30] E. Bols, J. Kieseler, M. Verzetti, M. Stoye and A. Stakia, *Jet Flavour Classification Using DeepJet*, *JINST* **15** (2020) P12012 [[2008.10519](#)].
- [31] H. Qu and L. Gouskos, *Jet tagging via particle clouds*, *Physical Review D* **101** (2020) 056019.
- [32] H. Qu, C. Li and S. Qian, *Particle Transformer for Jet Tagging*, [2202.03772](#).
- [33] Y. Wu, K. Wang, C. Li, H. Qu and J. Zhu, *Jet tagging with more-interaction particle transformer**, *Chinese Physics C* **49** (2025) 013110.
- [34] B.P. Roe, H.-J. Yang, J. Zhu, Y. Liu, I. Stancu and G. McGregor, *Boosted decision trees, an alternative to artificial neural networks*, *Nucl. Instrum. Meth. A* **543** (2005) 577 [[physics/0408124](#)].
- [35] H.-J. Yang, B.P. Roe and J. Zhu, *Studies of Boosted Decision Trees for MiniBooNE Particle Identification*, *Nucl. Instrum. Meth. A* **555** (2005) 370 [[physics/0508045](#)].
- [36] T. Chen and C. Guestrin, *Xgboost: A scalable tree boosting system*, in *Proceedings of the 22nd ACM SIGKDD International Conference on Knowledge Discovery and Data Mining*, KDD ’16, p. 785–794, ACM, Aug., 2016, [DOI](#).
- [37] F. An et al., *Precision higgs physics at the cepc*, *Chinese Physics C* **43** (2019) 043002.
- [38] A. Del Vecchio, J. Eysermans, L. Gouskos, G. Iakovidis, A. Maloizel, G. Marchiori et al., *Precision Measurements of Higgs Hadronic Decay Modes at the FCC-ee*, [2511.23149](#).
- [39] H. Yang, *Status of the CEPC Project*, *PoS ICHEP2024* (2025) 821.
- [40] X. Ai et al., *Flavor physics at the CEPC: a general perspective*, *Chin. Phys.* **49** (2025) 103003 [[2412.19743](#)].

- [41] S. Li et al., *Beam test of a baseline vertex detector prototype for cepc*, *IEEE Transactions on Nuclear Science* **71** (2024) 1319.
- [42] S. Song, J. Chen, J. Liu, Y. Liu, B. Qi, Y. Shi et al., *Study of residual artificial neural network for particle identification in the CEPC high-granularity calorimeter prototype*, *JINST* **19** (2024) P04033 [[2310.09489](#)].
- [43] W. Kilian, T. Ohl and J. Reuter, *Whizard—simulating multi-particle processes at lhc and ilc*, *The European Physical Journal C* **71** (2011) .
- [44] T. Sjöstrand, S. Mrenna and P. Skands, *Pythia 6.4 physics and manual*, *Journal of High Energy Physics* **2006** (2006) 026–026.
- [45] DELPHES 3 collaboration, *DELPHES 3, A modular framework for fast simulation of a generic collider experiment*, *JHEP* **02** (2014) 057 [[1307.6346](#)].
- [46] Y. Zhu, H. Cui and M. Ruan, *The higgs→ b \bar{b} , c \bar{c} , gg measurement at cepc*, *Journal of High Energy Physics* **2022** (2022) .
- [47] E. Bagnaschi, L. Biermann and M. Spira, *Higgs-Boson Decays: Updates*, [2510.24658](#).
- [48] H. Zhao, Y.-F. Zhu, C.-D. Fu, D. Yu and M.-Q. Ruan, *The higgs signatures at the cepc cdr baseline*, *Chinese Physics C* **43** (2019) 023001.
- [49] S. Catani, Y. Dokshitzer, M. Olsson, G. Turnock and B. Webber, *New clustering algorithm for multijet cross sections in e⁺e⁻ annihilation*, *Physics Letters B* **269** (1991) 432.
- [50] S. Lundberg and S.-I. Lee, *A unified approach to interpreting model predictions*, [1705.07874](#).
- [51] J. Shlens, *A tutorial on principal component analysis*, [1404.1100](#).
- [52] Y. Zhu, H. Liang, Y. Wang, Y. Che, H. Wang, C. Zhou et al., *Holistic approach and Advanced Color Singlet Identification for physics measurements at high energy frontier*, [2506.11783](#).
- [53] J. Altmann et al., *ECFA Higgs, electroweak, and top Factory Study*, vol. 5/2025 of *CERN Yellow Reports: Monographs* (6, 2025), [10.23731/CYRM-2025-005](#), [[2506.15390](#)].